Electric double-layer transistor using layered iron selenide Mott insulator TlFe$_{1.6}$Se$_2$

Takayoshi Katase[a,1], Hidenori Hiramatsu[b,c], Toshio Kamiya[b,c], and Hideo Hosono[a,b,c,2]

[a]Frontier Research Center, [b]Materials and Structures Laboratory, and [c]Materials Research Center for Element Strategy, Tokyo Institute of Technology, Yokohama 226-8503, Japan

A_{1-x}Fe$_{2-y}$Se$_2$ (A = K, Cs, Rb, Tl) are recently discovered iron-based superconductors with critical temperatures (T_c) ranging up to 32 K. Their parent phases have unique properties compared with other iron-based superconductors; e.g., their crystal structures include ordered Fe vacancies, their normal states are antiferromagnetic (AFM) insulating phases, and they have extremely high Néel transition temperatures. However, control of carrier doping into the parent AFM insulators has been difficult due to their intrinsic phase separation. Here, we fabricated an Fe-vacancy-ordered TlFe$_{1.6}$Se$_2$ insulating epitaxial film with an atomically flat surface and examined its electrostatic carrier doping using an electric double-layer transistor (EDLT) structure with an ionic liquid gate. The positive gate voltage gave a conductance modulation of three orders of magnitude at 25 K, and further induced and manipulated a phase transition; i.e., delocalized carrier generation by electrostatic doping is the origin of the phase transition. This is the first demonstration, to the authors' knowledge, of an EDLT using a Mott insulator iron selenide channel and opens a way to explore high T_c superconductivity in iron-based layered materials, where carrier doping by conventional chemical means is difficult.

field-effect devices | Fe-based superconductors

Layered copper-based oxides (cuprates) and iron-based superconductors are the most well-known types of superconductor because of their high critical temperatures (T_c) of more than 50 K (1, 2). One common feature of these materials is that superconductivity emerges when the long-range antiferromagnetic (AFM) order in the parent phase is suppressed and varnished by carrier doping. However, the maximum T_c of the cuprates (134 K for HgBa$_2$Ca$_2$Cu$_3$O$_{8+\delta}$) (3) is much higher than that of the iron-based materials [55 K for SmFeAs(O$_{1-x}$F$_x$)] (4). This difference is related to the different electron correlation interactions of the materials; i.e., the parent phases of the cuprates are AFM Mott insulators, where the electron–electron Coulomb interaction is very strong, whereas the iron-based parent phases are AFM metals with weaker electron correlation. Related to this difference, the Néel transition temperatures (T_N) of the cuprate parent phases (e.g., 420 K for YBa$_2$Cu$_3$O$_6$) (5) are much higher than those of the iron-based phases (e.g., 140 K for SmFeAsO) (6). Based on the high T_c cuprate scenario, it is considered that a key strategy to obtaining higher T_c in the iron-based superconductors is to dope carriers into the parent phase of a Mott insulator with a higher T_N and then disperse the magnetic order by carrier doping.

Recently, superconductivity was discovered at 32 K in a layered iron selenide, K$_{0.8}$Fe$_2$Se$_2$ (7), which has drawn considerable attention, because this is the first material with a parent phase to exhibit an AFM insulating state among the iron-based superconductors (8). The A_{1-x}Fe$_{2-y}$Se$_2$ (A = K, Cs, Rb, Tl) system has the same crystal structure as the 122-type iron-based superconductor BaFe$_2$As$_2$ with a tetragonal ThCr$_2$Si$_2$-type structure (9) (Fig. 1A), and is composed of alternately stacked A and FeSe layers along the c axis. The Fe atoms in the FeSe layer form a square lattice, where the Se atoms are located at the apical sites of the edge-shared FeSe$_4$ tetrahedra. However, the ideal chemical

formula is A_2Fe$_4$Se$_5$ (245 phase), which satisfies charge neutrality conditions with consideration of formal ion charges (i.e., +1 for A, +2 for Fe, and −2 for Se); therefore, the A and Fe sites include vacancies in the ThCr$_2$Si$_2$-type structure. It was shown that the Fe vacancies (V_{Fe}) in the parent 245 phase exhibit an order–disorder transition at ~500 K and form a $\sqrt{5} \times \sqrt{5} \times 1$ supercell (the unit cell formula is A_8Fe$_{16}$Se$_{20}$ with four V_{Fe}) (10), as shown in Fig. 1. Theoretical calculations suggested that the parent 245 phase is a Mott insulator with a Mott gap of ~100 meV (11, 12). The gap was confirmed experimentally to be ~430 meV (13). The 245 Mott insulator exhibits an AFM long-range order with T_N as high as 470–560 K, similar to that of the cuprates, along with an ordered magnetic moment of more than 3 Bohr magneton (μ_B) at 10 K (10). Because of this similarity to cuprates (i.e., a Mott insulator with high T_N), it is expected that a much higher T_c would be realized in a V_{Fe}-ordered AFM insulator of the 245 phase if the AFM order is suppressed by carrier doping.

Indeed, chemical electron-doping of the 245 phase has been performed by reducing the V_{Fe} (2 − y > 1.93), which induced superconductivity at ~30 K (8). However, it has been reported that these A_{1-x}Fe$_{2-y}$Se$_2$ superconductors intrinsically include phase separation into the superconducting phase, which is believed to exist in a phase without the V_{Fe} order, and the AFM-insulating phase (V_{Fe}-ordered 245 phase) (13). Further, there is controversy as whether the superconducting phase is an intercalated phase like Rb$_{0.3}$Fe$_2$Se$_2$ (14), a V_{Fe}-free phase like KFe$_2$Se$_2$ (13), or this disordered V_{Fe} phase (15). The coexistence of such multiphases indicates that a well-controlled carrier doping

Significance

One of the key strategies to obtaining higher superconducting critical temperature is to dope carriers into an antiferromagnetic Mott insulator with a high Néel temperature. Fe-vacancy-ordered A_{1-x}Fe$_{2-y}$Se$_2$ (A = K, Cs, Rb, Tl) is only one Mott insulator phase with extremely high Néel temperature among recently discovered iron-based superconductors. Here, we examined electrostatic carrier doping of the TlFe$_{1.6}$Se$_2$ insulator using an electric double-layer transistor structure. Three orders of magnitude modulation of channel conductance was observed, and the phase transition was induced by gate voltage, which indicates that delocalized carrier generation by electrostatic doping is its origin. This result opens a way to explore high critical temperature superconductivity in iron-based layered materials, where carrier doping by conventional chemical means is difficult.
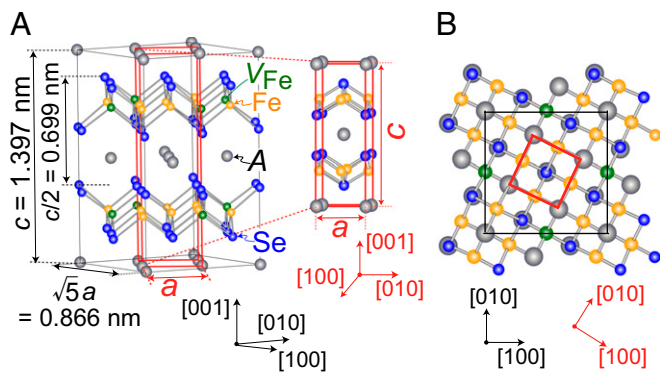
PHYSICS

Fig. 1. Crystal structures of 122-type $A_{1-x}Fe_{2-y}Se_2$ (A = K, Cs, Rb, Tl) and 245-type parent-phase $A_2Fe_4Se_5$ viewed along the [120] (*A*) and the [001] (*B*) directions. The spheres represent A (gray), Fe (orange), Se (blue), and Fe vacancy sites (V_{Fe}, green). The 122-type tetragonal fundamental cell and the 245-type $\sqrt{5} \times \sqrt{5} \times 1$ supercell are indicated by the red and black lines, respectively.

structure of the 245 phase has yet to be realized by chemical-composition doping or substitution, and the carrier doping effects are not yet clear. In contrast, carrier doping by an electrostatic method that uses a field-effect transistor structure is free from this structural alternation and would be suitable for study of phase transitions in V_{Fe}-ordered 245 Mott insulators that have never become a superconductor.

In this study, we focused on the epitaxial films of one iron selenide Mott insulator, $TlFe_{1.6}Se_2$, because $TlFe_{2-y}Se_2$ is much more stable in air than the other $A_{1-x}Fe_{2-y}Se_2$ (A = K, Rb, Cs) (16), and a fully V_{Fe}-ordered phase with high chemical homogeneity has been obtained in single crystals due to the lower vapor pressure of Tl than those of alkaline metals (17). In addition, the number of V_{Fe} in $TlFe_{2-y}Se_2$ cannot be controlled over a wide range (the maximum $2 - y$ value is limited to only 1.6) regardless of the starting nominal compositions, and thus superconductivity has not previously been observed in $TlFe_{1.6}Se_2$ (16), although a bulk superconductivity was observed in mixed $(Tl,K)_{1-x}Fe_{2-y}Se_2$ (18). These features demonstrate that the $TlFe_{1.6}Se_2$ AFM insulator is the most ideal target to examine electrostatic carrier doping. We therefore used an electric double-layer transistor (EDLT) structure because the ionic liquid gate works as a nanometer-thick capacitor with a large capacitance and provides an effective way to accumulate a very high carrier density [maximum sheet carrier density of $\sim 10^{15}$ cm^{-2} under small gate voltages (V_G) of around ± 3 V]. This high carrier modulation by the EDLT can alter electronic states over a very wide range and convert even a band insulator into a metal, and even further, into a superconductor (19); similarly, a Mott insulator can be converted into a metal (20). We therefore expected that the EDLT structure would also modulate the carrier density sufficiently to induce a phase transition such as superconductivity in the iron selenide Mott insulator without chemical doping or structural alternation. Here, we used a single phase (i.e., homogeneous in structure, chemical composition, and vacancy distribution) and V_{Fe}-ordered $TlFe_{1.6}Se_2$ insulating epitaxial film grown by pulsed laser deposition (PLD) with an atomically flat surface as the transport channel layer of the EDLT. Large field-effect current modulation was demonstrated in the EDLT, particularly at low temperatures. The electric field clearly decreased the activation energy (E_a) and also induced a phase transition.

Fig. 2*A* shows the out-of-plane X-ray diffraction (XRD) pattern of a $TlFe_{1.6}Se_2$ thin film grown at the optimum temperature of 600 °C. Only the sharp peaks of the 00*l* diffractions of the $TlFe_{1.6}Se_2$ phase were observed, along with those of the CaF_2

substrate, indicating that the film grows along the [00*l*] direction. Although the in-plane lattice parameter of CaF_2 ($a/\sqrt{2} = 0.386$ nm) is almost the same as that of $(La,Sr)(Al,Ta)O_3$ (LSAT) ($a/2 = 0.387$ nm), the full width at half maximum (FWHM) values of the 004 rocking curve ($\Delta\omega$) of the film are much smaller when grown on the CaF_2 substrate (0.08°) than that grown on the LSAT substrate (0.8°) (Fig. 2*B*). This suggests that an interface reaction occurs on the oxide LSAT substrate, whereas the fluoride CaF_2 substrate is more suitable for $TlFe_{1.6}Se_2$; similar results are reported also for iron chalcogenide $FeSe_{0.5}Te_{0.5}$ epitaxial films (21). To confirm the epitaxial relationship between the $TlFe_{1.6}Se_2$ film and the CaF_2 substrate, asymmetric diffractions were measured. Fig. 2*C* shows the results of ϕ scans of the 123 diffraction of the $TlFe_{1.6}Se_2$ film and the 202 diffraction of the CaF_2 substrate. Both peaks appear every 90° and exhibit fourfold symmetry, substantiating the heteroepitaxial nature of the $TlFe_{1.6}Se_2$ film growth on the CaF_2 substrate. Each peak (FWHM value = 0.2°) of the $TlFe_{1.6}Se_2$ film is rotated by 45° with respect to the peaks of the CaF_2 substrate, showing that the $TlFe_{1.6}Se_2$ film grows on the CaF_2 substrate with epitaxial relationships of [001] $TlFe_{1.6}Se_2$//[001] CaF_2 (out of plane) and [310] $TlFe_{1.6}Se_2$//[100] CaF_2 (in plane). These epitaxial relationships are a natural consequence of the smallest in-plane lattice mismatching [$\Delta(d_{Tl-Tl} - d_{Ca-Ca})/d_{Ca-Ca} \times 100 = 0.8\%$] as shown in Fig. 2*D*. Fig. 2*E* shows the surface morphology of the $TlFe_{1.6}Se_2$ epitaxial film on the CaF_2 substrate. A flat surface with a step-and-terrace structure (root-mean-square roughness of 1.4 nm) was observed, indicating the layer-by-layer growth of $TlFe_{1.6}Se_2$ epitaxial films under
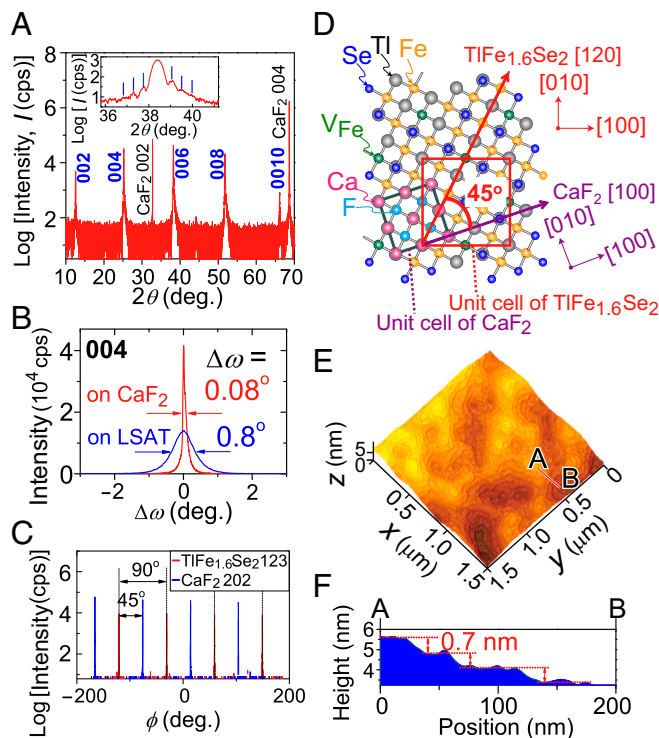

Fig. 2. (*A*) Out-of-plane XRD pattern of a $TlFe_{1.6}Se_2$ film grown on a CaF_2 (001) substrate. (*A, Inset*) The magnified pattern around the 006 diffraction. The vertical lines indicate the positions of the Pendellösung interference fringes. (*B*) Rocking curves of the 004 diffractions of the $TlFe_{1.6}Se_2$ films on CaF_2 and LSAT substrates. (*C*) ϕ scans of the 123 diffraction of the $TlFe_{1.6}Se_2$ film and the 202 diffraction of the CaF_2 substrate. (*D*) In-plane atomic configuration of the $TlFe_{1.6}Se_2$ epitaxial film on the CaF_2 substrate. (*E*) Topographic atomic force microscopy image of the surface of the $TlFe_{1.6}Se_2$ epitaxial film on the CaF_2 substrate. (*F*) Height profile across the line A–B shown in *E*.

Katase et al.

optimized conditions. This result is also consistent with the observation of Pendellösung interference fringes (Fig. 2A, Inset). The step height (Fig. 2F) observed by atomic force microscopy is ~0.7 nm, which agrees well with the distance between the nearest-neighbor FeSe–FeSe layers [corresponding to a half unit of the c-axis length (1.397 nm) of the $TlFe_{1.6}Se_2$ unit cell indicated in Fig. 1A]. These results guarantee that the $TlFe_{1.6}Se_2$ epitaxial film is of sufficiently high quality to be used for the EDLT transport channel.

The atomic structure and V_{Fe} ordering in the $TlFe_{1.6}Se_2$ epitaxial film were examined by high-angle annular dark field scanning transmission electron microscopy (HAADF-STEM) and selected area electron diffraction (SAED). Fig. 3 A and B show the plan-view HAADF-STEM images of the $TlFe_{1.6}Se_2$ epitaxial film. V_{Fe} are detected as the dark regions due to the enhanced atomic number contrast of HAADF, showing the long-range periodic V_{Fe} ordering. In addition, superlattice diffractions due to the V_{Fe} ordering, similar to that of $TlFe_{1.6}Se_2$ single crystal (17), were observed in the SAED pattern Fig. 3C as indicated by q_1 and q_2. These results substantiate that the present sample is of a highly V_{Fe}-ordered phase. Fig. 3D demonstrates the arrangement of V_{Fe} more clearly by superimposing yellow lines on the HAADF-STEM image of Fig. 3A. Fully ordered V_{Fe} are dominant in almost the whole region, while small phase separation to disordered-V_{Fe} regions ≤5 nm in size (the unmarked regions in Fig. 3D) were also observed by keeping the perfect coherency of the fundamental crystal structure.

A 20 nm-thick $TlFe_{1.6}Se_2$ epitaxial film was used as the EDLT transport channel. Fig. 4 shows a schematic illustration of the EDLT, in which a six-terminal Hall bar channel and Au pad electrodes were formed using shadow masks. After pouring the ionic liquid, N,N-diethyl-N-methyl-N-(2-methoxyethyl)-ammonium bis-(trifluoromethylsulfonyl) imide (DEME-TFSI), into a silica glass cup, a Pt coil electrode was inserted into the ionic liquid to act as
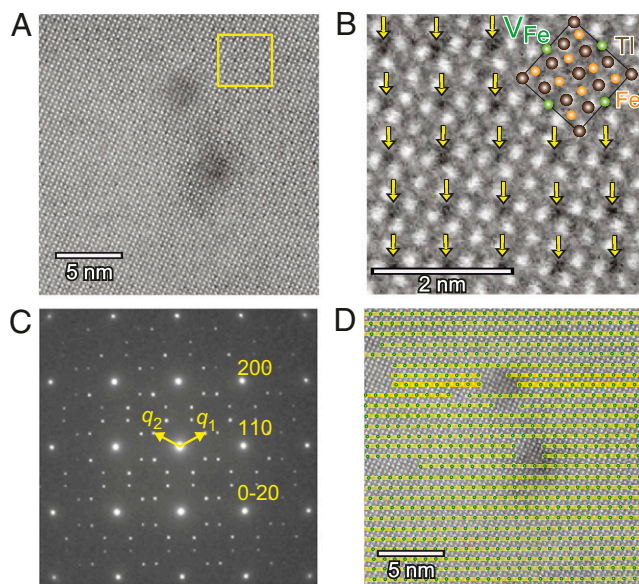

Fig. 4. Schematic of the EDLT using $TlFe_{1.6}Se_2$ epitaxial film with a six-terminal Hall bar structure on a CaF_2 substrate. V_G was applied via a Pt counter electrode through the ionic liquid, DEME-TFSI, contained in a silica glass cup. Electrical contacts were formed using Au wires and In/Au pads.

a gate electrode. The transfer curves [V_G dependence of drain current (I_D)] at a drain voltage (V_D) of +0.3 V and output curves (I_D vs. V_D under various V_G) of the EDLT were then measured.

Fig. 5A shows the cyclic transfer characteristics (I_D vs. V_G) of the $TlFe_{1.6}Se_2$ EDLT at T = 280 K. A positive V_G of up to +4 V was applied to the Pt coil gate electrode, which accumulates electrons at the interface. When V_G = +1.7 V was applied, I_D began to increase. The maximum I_D in the transfer curve reached 12 μA at V_G = +4 V, along with a small on:off ratio of 1.5. The gate leakage current (I_G) (Fig. 5A, Lower) also increased at V_G up to +4.0 V but was clearly smaller than I_D in the whole V_G region. After applying V_G = +4 V, I_D recovered to the initial values of 8 μA when V_G was decreased to 0 V. The large hysteresis loop is observed due to the slow response of ion displacement in the ion liquid. Probably due to the same reason, some parallel shift remains in the second I_D–V_G loop; however, the shape and the hysteresis width are very similar to those of the first loop, guaranteeing the observed results are reversible and reproducible. These results demonstrate the electrostatic nature of carrier accumulation. In the output characteristics (Fig. 5B), the conductance dI_D/dV_D increased with increasing V_G at ≥ +2.0 V. Two output characteristics, which were measured before and after the transfer curve measurements in Fig. 5A, remain unchanged, which further guarantees the reversibility of the EDLT characteristics. However, the I_D modulation is small at 280 K because of the high conductance at V_G = 0, which originates from the highly naturally doped carriers in the $TlFe_{1.6}Se_2$ film, as reported for a $TlFe_{1.6}Se_2$ bulk crystal in which the carrier density was estimated to be ~5×10^{21} cm^{-3} at T = 150 K (16). Using the reported gate capacitance value of ~10 μF/cm^2 (22), the maximum accumulated carrier density is estimated to be 2.5×10^{14} cm^{-2} at V_G = 4 V, and the field-effect mobility in the linear region of the output characteristics is estimated to be 0.18 cm^2/(V·s) at V_G = +4 V. To estimate the carrier density induced in the $TlFe_{1.6}Se_2$ EDLT, we performed Hall effect measurements by applying magnetic fields of up to 9 T at temperatures between 300 and 25 K, but the Hall voltages (V_{xy}) obtained were below the detection limit of our measurement system. This suggests that the Hall mobility is smaller than 0.02 cm^2/(V·s), which is roughly consistent with the small field-effect mobility above. Fig. 5C plots the V_G dependence of the sheet conductance (G_s) at T = 300–25 K. The V_G dependences of G_s were reversible also against repeated variation of measurement temperature (compare the open symbols and the filled symbols in Fig. 6A). With decreasing T, G_s at V_G = 0 V steeply decreased from 2.2×10^{-5} to 1.5×10^{-8} S because of the decrease in carrier density. It should be noted that large G_s modulation with gains of three orders of magnitude was demonstrated at T = 25 K.

Fig. 3. (A) [001] plan-view HAADF-STEM image of $TlFe_{1.6}Se_2$ epitaxial film. (B) Magnified HAADF-STEM image of the yellow square region in A. Vertical yellow arrows indicate the V_{Fe} sites with dark contrast. (B, Inset) The crystal structure of $TlFe_{1.6}Se_2$, where only Tl and Fe sites are shown because the positions of Se and Tl sites overlap over them (Fig. 1B). The square shows the superlattice unit cell, where V_{Fe} are shown (green circles). (C) The SAED pattern with electron beam along [001]. Two superlattice reciprocal vectors due to V_{Fe} ordering are indexed by q_1 and q_2. (D) Small green circles indicate all detected V_{Fe}, and yellow lines indicate V_{Fe} arrangement.
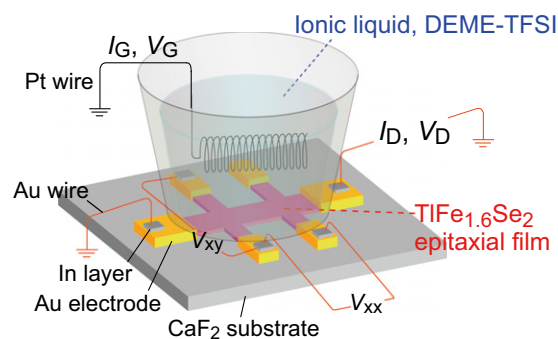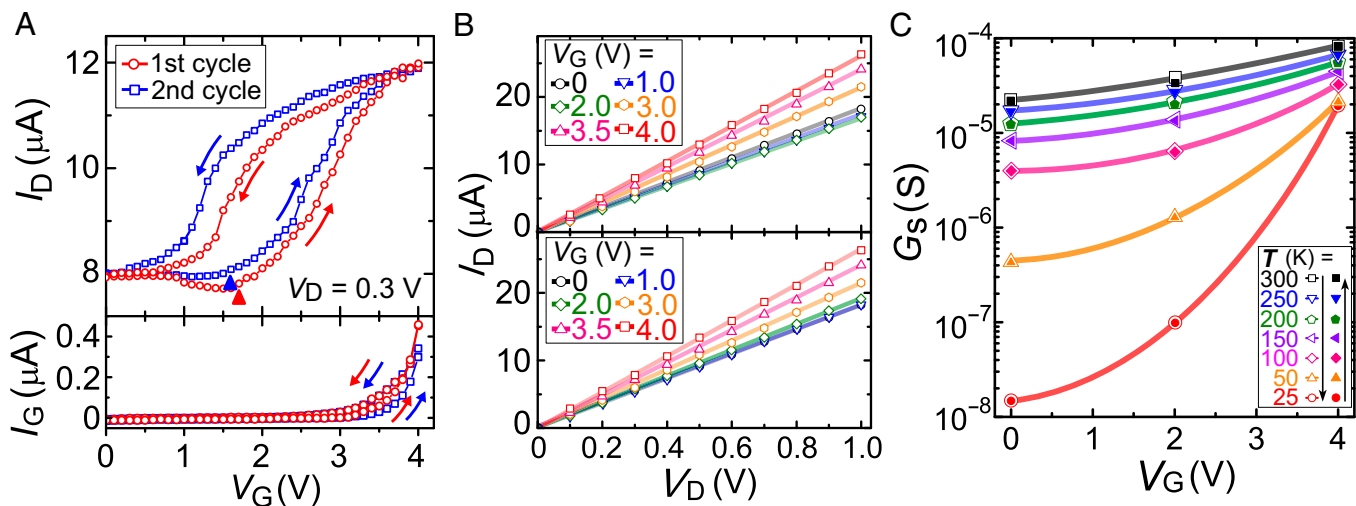
Fig. 5. (*A*) Transfer characteristics (I_D–V_G) at V_D = +0.3 V and T = 280 K cyclically measured for two loops. Arrows indicate the V_G sweep directions, and triangles show the positions where I_D begins to increase. I_G vs. V_G is also shown at the bottom. (*B*) Output characteristics (I_D–V_D) at V_G = + 0–4 V and T = 280 K, measured before (*Upper*) and after (*Lower*) the transfer characteristics measurement in *A*. (*C*) V_G dependence of G_s measured with decreasing T (open symbols) and increasing T (filled symbols) over the 25–300 K range. The solid lines are visual to show the change in G_s clearly.

Fig. 6*A* shows the T dependences of the sheet resistance R_s (R_s–T) for the TlFe$_{1.6}$Se$_2$ EDLT at V_G = 0, +2, and +4 V. The R_s–T characteristics from 300 to 30 K at V_G = 0 V indicate simple thermally activated behavior, given by $R_s = R_{s0} \exp(E_a/k_B T)$ (where R_{s0} is a constant and k_B is the Boltzmann constant). This trend is similar to the R_s–T behavior of insulating TlFe$_{2-y}$Se$_2$ single crystals with $2 - y < 1.5$ (18), but the resistivity anomaly due to a magnetic phase transition of spin reorientation at 100 K observed in the TlFe$_{1.6}$Se$_2$ single crystal (16, 17) was not detected. The E_a value of the TlFe$_{1.6}$Se$_2$ EDLT at V_G = 0 obtained from the Arrhenius fitting is 20 meV (Fig. 6*B*). This value is smaller than the 57.7 meV of the TlFe$_{1.47}$Se$_2$ single crystal (18) but almost double that of TlFe$_{1.6}$Se$_2$ single-crystals (11 meV) (16). These observations indicate the naturally doped carrier density should be smaller than that of the TlFe$_{1.6}$Se$_2$ single crystals. On the other hand, E_a is far smaller than the calculated (~100 meV) (11, 12) and experimentally measured Mott gaps (~430 meV) (13), which suggests that the TlFe$_{1.6}$Se$_2$ film is doped with carriers.

The R_s–T behavior largely varied with V_G, particularly in the low T region, which is seen also in Fig. 5*C*. The R_s–T curves were reversible in the cooling and heating cycles. The E_a value estimated in the high T region decreased from ~20 meV at V_G = 0–2 V to 8.9 meV at V_G = +4 V (Fig. 6*B*); i.e., R_s at V_G = +4 V is almost independent of T, indicating that a highly accumulated channel was formed by the application of V_G. The R_s–T curves at $V_G \geq 2$ V do not show a simple thermally activated behavior and exhibit humps at T = 55 K for V_G = +2 V and at 40 K for V_G = +4 V (indicated by the vertical arrows in Fig. 6*A*). That is, when V_G was increased from 0 to +2 V, the resistance hump appeared at T_{hump} = 55 K, and R_s increased steeply again at $T \leq 31$ K. At V_G = +4 V, T_{hump} shifted to a lower T (40 K), and R_s leveled off in the further lower T region. It would be possible to consider that the resistivity humps are attributed to a precursory phenomenon of a metal–insulator (MI) transition because E_a decreased sharply as confirmed in Fig. 6*B*. As for the A_{1-x}Fe$_{2-y}$Se$_2$ superconductor single crystals, they also exhibit resistance humps and cross-overs from an insulating state to a metallic state at T_{hump}, and finally to a superconducting state (18). In the case of (Tl,K) Fe$_{2-y}$Se$_2$ in the literature (Fig. 6*A*, *Inset*) (18), the resistance hump appears at $2 - y$ = 1.68, and the superconductivity appears at $2 - y \geq 1.76$. This value is 16% larger than that of the TlFe$_{1.6}$Se$_2$ film in this work. This preceding work suggests that the T_{hump} observed in this study can also be related to the MI

transition and superconductivity; however, in this study we could not observe superconductivity up to the maximum V_G of +4 V.

A similar phenomenon, which is attributed to a magnetic phase transition, has been observed also in fully V_{Fe}-ordered (100 K) (17) and multiphase (100–150 K) (23) TlFe$_{1.6}$Se$_2$ single crystals. On the other hand, the resistance humps are attributed to the formation of an orbital-selective Mott phase (OSMP) for the V_{Fe}-poor A_{1-x}Fe$_{2-y}$Se$_2$ bulk crystals, where one of the Fe 3d orbitals, d_{xy}, remains localized and the other four orbitals are delocalized (24, 25). The Mott insulator phase dominates the resistance above T_{hump}, whereas the OSMP prevails below it; finally, superconductivity
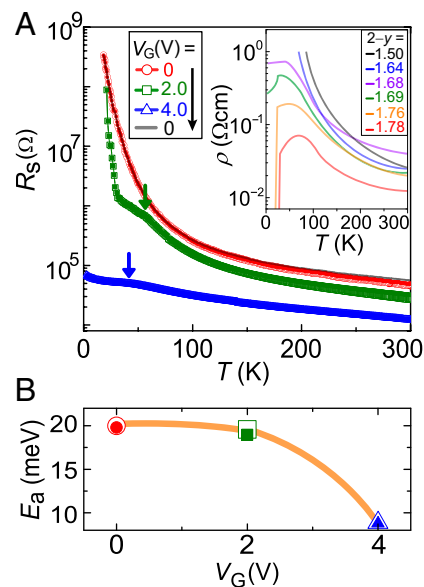

Fig. 6. (*A*) T dependences of R_s for the TlFe$_{1.6}$Se$_2$ EDLT measured with increasing T (open symbols) and decreasing T (filled symbols) at V_G = 0→+ 2.0→+4.0→0 V. The arrows indicate the positions of resistance humps. The reported ρ–T curves of (Tl,K) Fe$_{2-y}$Se$_2$ bulk materials (18) are shown for comparison (*Inset*). A resistance hump appears at $2 - y \geq 1.68$, and superconductivity emerges at $2 - y \geq 1.76$. (*B*) The E_a estimated from *A* in the high T region as a function of V_G.

Katase et al.

appears below T_{hump} of the OSMP transition at higher carrier doping levels. Due to these similarities, we consider that the resistance humps observed in this study are more likely assigned to the same origin of magnetic phase transition or OSMP.

In summary, electrostatic carrier doping of the Mott insulator iron selenide V_{Fe}-ordered $TlFe_{1.6}Se_2$ by the EDLT structure was demonstrated using a single-phase epitaxial film with an atomically flat surface grown on a CaF_2 substrate. The EDLT structure, based on an ionic liquid gate, successfully controlled the conductance and induced the phase transition assignable to a magnetic phase transition or OSMP. This demonstration of carrier doping of the Mott insulator iron selenide by the electrostatic method offers a way to extend the exploration of high T_c superconductors even to insulating materials, in which chemical doping methods do not work.

Experiments

Film Growth and Characterization. Epitaxial films of $TlFe_{1.6}Se_2$ were grown on fluorite-type CaF_2 and mixed perovskite-type LSAT (001) single crystals by PLD. A KrF excimer laser (wavelength of 248 nm) was used to ablate a $TlFe_{1.6}Se_2$ polycrystalline target disk, which was synthesized using a two-step solid-state reaction. Fine pieces of the Tl metal and powders of FeSe and Se were mixed in a stoichiometric atomic ratio of Tl:FeSe:Se = 1:1.6:0.4 and sealed in an Ar-filled stainless steel tube. The mixture was first reacted at 400 °C for 5 h, and then at 650 °C for 10 h. The resulting powders were ground thoroughly and pressed into pellets, which were then placed in Ar-filled stainless steel tubes and heated at 650 °C for 16 h. All PLD target fabrication procedures except the heating process were carried out in an Ar-filled glove box. The base pressure of the PLD growth chamber used in this study was $\sim10^{-5}$ Pa. The laser energy fluence and the repetition rate were 10 J/cm^2 and 10 Hz, respectively. When grown in the 300–550 °C temperature range, epitaxial films were obtained, but their surfaces were relatively rough because of the 3D growth mode, whereas the FeSe impurity phase was detected at temperatures ≥650 °C. Thus, we concluded that the optimal growth temperature was 600 °C.

The film structures, including crystalline quality and the orientation of the crystallites, were examined by XRD (anode radiation: monochromatic CuKα$_1$).

The film thickness was characterized by X-ray reflectivity. The chemical composition of the film was checked by X-ray fluorescence measurements and electron probe microanalyzer (EPMA), and confirmed that the film's chemical composition was the same as that of the PLD target. EPMA mapping indicated that composition of the epitaxial films was homogeneous with a spatial resolution of a few micrometers. The surface morphology of the film was measured with an atomic force microscope. The microstructure of V_{Fe} ordering in $TlFe_{1.6}Se_2$ epitaxial films was examined by HAADF-STEM and SAED. The STEM sample was prepared with a focused ion beam system. All these characterization measurements were performed at room temperature.

Device Fabrication and Characterization of Electrical Properties. The 20 nm-thick $TlFe_{1.6}Se_2$ epitaxial films on the CaF_2 (001) substrate were used as the transport channel of the EDLT. The $TlFe_{1.6}Se_2$ channel layer with a six-terminal Hall bar geometry (channel size: 500 μm long and 200 μm wide) and the Au pad electrodes were deposited using shadow masks. After bonding Au wires to the Au pads with In, a silica glass cup was placed on the devices and the Au wires were fixed with an epoxy adhesive. We used an ionic liquid, DEME-TFSI, as the medium for the gate electrode because it has a wide electrochemical potential window that extends up to +4 V and is free from water, which means that it is suitable for application to the EDLT. The ionic liquid was used to fill the silica glass cup and then a Pt coil was inserted into the ionic liquid to act as the gate electrode.

Transfer curves (i.e., the V_G dependence of I_D) and the output curves (I_D vs. V_D under various values of V_G) were taken from the results gathered by a source measurement unit. The T dependence of R_s was measured by the four-probe method over a T range of 2–300 K. Because DEME-TFSI exhibits a glass transition from a rubber phase to a glass phase at $T = 190$ K, and the ion motion is frozen out at lower values of T, V_G was applied at 300 K to form a highly accumulated gate structure, and then T was reduced while maintaining the same V_G (26).

1. Bednorz JG, Müller KA (1986) Possible high T_c superconductivity in the Ba-La-Cu-O system. *Z Phys B* 64(2):189–193.
2. Kamihara Y, Watanabe T, Hirano M, Hosono H (2008) Iron-based layered superconductor La[O$_{1-x}$F$_x$]FeAs (x = 0.05-0.12) with T_c = 26 K. *J Am Chem Soc* 130(11):3296–3297.
3. Schilling A, Cantoni M, Guo JD, Ott HR (1993) Superconductivity above 130 K in the Hg-Ba-Ca-Cu-O system. *Nature* 363(6424):56–58.
4. Ren ZA, et al. (2008) Superconductivity at 55 K in iron-based F-doped layered quaternary compound Sm[O$_{1-x}$F$_x$]FeAs. *Chin Phys Lett* 25(6):2215–2216.
5. Tranquada JM, et al. (1988) Antiferromagnetism in YBa$_2$Cu$_3$O$_{6+x}$. *Phys Rev B* 38(4):2477–2485.
6. Drew AJ, et al. (2009) Coexistence of static magnetism and superconductivity in SmFeAsO$_{1-x}$F$_x$ as revealed by muon spin rotation. *Nat Mater* 8(4):310–314.
7. Guo J, et al. (2010) Superconductivity in the iron selenide K$_x$Fe$_2$Se$_2$ (0≤x≤1.0). *Phys Rev B* 82(18):180520.
8. Yan YJ, et al. (2012) Electronic and magnetic phase diagram in K$_x$Fe$_{2-y}$Se$_2$ superconductors. *Sci Rep* 2:212.
9. Rotter M, Tegel M, Johrendt D (2008) Superconductivity at 38 K in the iron arsenide (Ba$_{1-x}$K$_x$)Fe$_2$As$_2$. *Phys Rev Lett* 101(10):107006.
10. Ye F, et al. (2011) Common crystalline and magnetic structure of superconducting A_2Fe$_4$Se$_5$ (A=K,Rb,Cs,Tl) single crystals measured using neutron diffraction. *Phys Rev Lett* 107(13):137003.
11. Yu R, Zhu JX, Si Q (2011) Mott transition in modulated lattices and parent insulator of (K,Tl)$_y$Fe$_x$Se$_2$ superconductors. *Phys Rev Lett* 106(18):186401.
12. Yan XW, Gao M, Lu ZY, Xiang T (2011) Electronic structures and magnetic order of ordered-Fe-vacancy ternary iron selenides TlFe$_{1.5}$Se$_2$ and AFe$_{1.5}$Se$_2$ (A=K, Rb, or Cs). *Phys Rev Lett* 106(8):087005.
13. Li W, et al. (2012) Phase separation and magnetic order in K-doped iron selenide superconductor. *Nat Phys* 8(2):126–130.
14. Texier Y, et al. (2012) NMR study in the iron-selenide Rb$_{0.74}$Fe$_{1.6}$Se$_2$: Determination of the superconducting phase as iron vacancy-free Rb$_{0.3}$Fe$_2$Se$_2$. *Phys Rev Lett* 108(23):237002.
15. Chen F, et al. (2011) Electronic identification of the parental phases and mesoscopic phase separation of K$_x$Fe$_2$Se$_2$ superconductors. *Phys Rev X* 1(2):021020.
16. Sales BC, et al. (2011) Unusual phase transitions and magnetoelastic coupling in TlFe$_{1.6}$Se$_2$ single crystals. *Phys Rev B* 83(22):224510.
17. May AF, et al. (2012) Spin reorientation in TlFe$_{1.6}$Se$_2$ with complete vacancy ordering. *Phys Rev Lett* 109(7):077003.
18. Fang MH, et al. (2011) Fe-based superconductivity with T_c=31 K bordering an antiferromagnetic insulator in (Tl,K) Fe$_x$Se$_2$. *Europhys Lett* 94(2):27009.
19. Ueno K, et al. (2008) Electric-field-induced superconductivity in an insulator. *Nat Mater* 7(11):855–858.
20. Nakano M, et al. (2012) Collective bulk carrier delocalization driven by electrostatic surface charge accumulation. *Nature* 487(7408):459–462.
21. Tsukada I, et al. (2011) Epitaxial growth of FeSe$_{0.5}$Te$_{0.5}$ thin films on CaF$_2$ substrates with high critical current density. *Appl Phys Express* 4(5):053101.
22. Ye JT, et al. (2010) Liquid-gated interface superconductivity on an atomically flat film. *Nat Mater* 9(2):125–128.
23. Cao H, et al. (2012) Evolution of the nuclear and magnetic structures of TlFe$_{1.6}$Se$_2$ with temperature. *Phys Rev B* 85(5):054515.
24. Yi M, et al. (2013) Observation of temperature-induced crossover to an orbital-selective Mott phase in A_xFe$_{2-y}$Se$_2$ (A = K, Rb) superconductors. *Phys Rev Lett* 110(6):067003.
25. Yu R, Si Q (2013) Orbital-selective Mott phase in multiorbital models for alkaline iron selenides K$_{1-x}$Fe$_{2-y}$Se$_2$. *Phys Rev Lett* 110(14):146402.
26. Yuan HT, et al. (2009) High-density carrier accumulation in ZnO field-effect transistors gated by electric double layers of ionic liquids. *Adv Funct Mater* 19(7):1046–1053.

PHYSICS